Sensitivity of the Stribeck curve to the pin geometry of a pin-on-disc tribometer*

Erik Hansen*

Institute of Fluid Mechanics, Karlsruhe Institute of Technology (KIT), Kaiserstr. 10, 76131 Karlsruhe, Germany

Bettina Frohnapfel

Institute of Fluid Mechanics, Karlsruhe Institute of Technology (KIT), Kaiserstr. 10, 76131 Karlsruhe, Germany

Andrea Codrignani

Department of Microsystems Engineering, Albert-Ludwigs-University Freiburg, Georges-Köhler-Allee 103, 79110 Freiburg, Germany

Abstract

A considerable number of surface texture investigations is based on pin-on-disc tribometers. This work shows that a crucial role in the reproducibility of the results, *e.g.* Stribeck curves, is played by the geometry of the pin surface. The investigation is based on an elastohydrodynamic model of a pin-on-disc tribometer which is validated with experimental data. Characteristic roughness and pin shapes are introduced in this model to evaluate the sensitivity of the Stribeck curve to these operating conditions. The obtained significant variations in the friction coefficient indicate that studies which aim at quantifying the influence of surface textures in the mixed lubrication regime need to provide information about the pin geometry in order to enable a meaningful comparison among literature data.

Keywords: mixed lubrication, modelling in tribology, pin-on-disc

*This document is the result of a research project funded by the Friedrich und Elisabeth Boysen-Foundation.

*Corresponding author

Email address: erik.hansen@kit.edu (Erik Hansen)

URL: www.istm.kit.edu (Erik Hansen)

tribometer, surface texturing

1. Introduction

Since 20% of the world's total energy consumption goes to overcome friction [1], research on drag reduction bears great potential in energy saving. One of these technologies is the introduction of surface textures in lubricated contacts. Surface textures in the shape of dimples can cause an additional pressure build-up within the lubrication flow, which leads to a thicker fluid film and less friction [2]. This positive effect is highly sensitive to the contact's operating condition and the robust and versatile design is a subject of intensive research [3, 4]. Due to the high sensitivity of the texture parameters, the operating conditions during their investigations must be known and controlled. A widely used way to investigate surface textures under such isolated conditions is the pin-on-disc tribometer [5]. The knowledge of all operating parameters in this experiment allows its numerical representation, while the experimental results enable the meaningful validation of the created digital twin. Among others, such studies were previously carried out in the context of a thrust bearing [6] or a piston-ring-liner contact [7]. In the case of a pin-on-disc tribometer, setting up a digital twin based on previously published experimental data proves to be difficult because important information, such as the measurement of the pin curvature, is often missing [8, 9, 10, 11, 12, 13]. For the present study additional data of the pin geometry employed in the experiments of Braun *et al.* [8] is used in order to determine the sensitivity of numerical predictions on this quantity. In consequence, a suggestion of the surface parameters that should be published along with experimental results can be made.

The paper is structured as follows. The reference pin-on-disc tribometer is introduced in section 2 before the setup of the corresponding numerical model is explained in section 3. This model is based on a two-scale approach in which the roughness scale is considered through precalculated contact pressure and homogenization factors [14] while the modelling of the elastohydrodynamic lubrication (EHL) is performed through the homogenized Reynolds equation including mass-conserving cavitation [5, 15, 16] and the boundary element method [17]. In section 4, the implemented model is used to quantify the influence of the pin geometry on the Stribeck curve.

2. Reference Tribometer set-up

A schematic setup of the Plint TE-92 HS tribometer from Phoenix Tribology (Kingsclere, UK) that was used for the experiments of Braun *et al.* [8] is depicted in Figure 1. It shows the rotating disc that is pressed with the normal force F_N against the pin. The pin is placed on a self alingning pin holder and the contact of pin and disc is constantly fed with oil. The setup is heated to keep the oil temperature at 100°C. At this temperature, the additive free poly-alpha-olefin (PAO), Klüber Lubrication (Munich, Germany) has a dynamic viscosity of approximately $\mu_l = 0.0031$Pa·s. The pin with a diameter of 8mm consists of normalized steel C85 (Stahlbecker, Heusenstamm, Germany) with a Young's modulus of approximately $E = 206$GPa and a hardness of 400HV. The disc with a diameter of 70mm is made out of hardened and tempered (190°C) steel 100Cr6 (AISI 5210, Eisen Schmitt, Karlsruhe, Germany) with a hardness of 800HV.

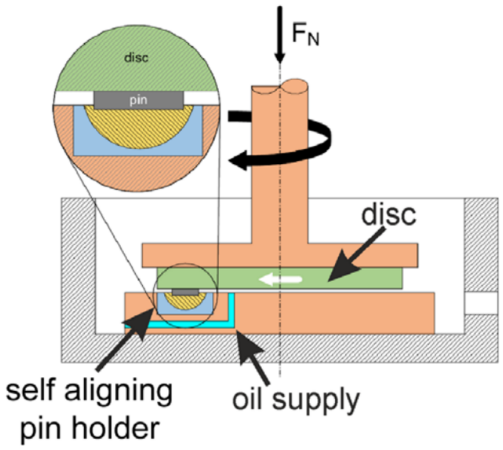

Figure 1: Schematic set-up of the pin-on-disc tribometer as presented in [8].

During the experiments, the friction force F_T acting on the pin surface is measured to determine the friction coefficient C_f [18]:

$$C_f = \frac{F_T}{F_N}. \tag{1}$$

The Stribeck curve is measured for different disc velocites U by approximating them as $U = \Omega \cdot r_s$, where Ω is the angular velocity of the disc and

$r_s = 30$mm is the distance from the pin center to the rotation center of the disc. Consequently, this approximation neglects velocity gradient effects [19].

In order to numerically reproduce the experimental Stribeck curve, the forces F_N and F_T on the pin surface A must be computed. This is performed by superposition of the hydrodynamic, ambient and contact pressures, p_{hd}, p_a and p_c, and the corresponding shear stresses, τ_{hd} and τ_c [5]:

$$F_N = \int_A p_{tot} \mathrm{d}A = \int_A (p_{hd} - p_a + p_c)\, \mathrm{d}A, \tag{2}$$

$$F_T = \int_A \tau_{tot} \mathrm{d}A = \int_A (\tau_{hd} + \tau_c)\, \mathrm{d}A. \tag{3}$$

Realistic values for these two quantities need to be determined in order to study the influence of pin surface geometry and pin roughness in the digital twin of the experiment. Unfortunately, this geometrical information is typically not provided in literature.

As reference for the present study we complement the results of Braun *et al.* [8] with additional measurement data that are accessible. The additional data consist of a macroscopic and microscopic surface measurement of the pin from the experiments and was provided by the Institute of Applied Materials - Computational Materials Science at the Karlsruhe Institute of Technology where the original experiments were conducted. The data is also published in the supplements of the present work. For the macroscopic pin profile, a surface measurement along the centerline of an unused pin is considered and extrapolated. The result is presented in Figure 2 where rounding of the pin surface is clearly visible. This macroscopic surface geometry originates from the polishing step during manufacturing. It should be noted that this pin surface has not yet been subjected to wear and running in effects which are likely to generate geometrical changes. Therefore, the available surface geometry can only serve as a rough estimate of the maximum gap height variations across the pin.

In contrast to the macroscopic pin geometry, information about the pin roughness is available for used pins. The roughness profile on a run-in pin was measured with an optical 3D-profilometer of the type PLu from SensoFar (Barcelona, Spain) in an interferometric measuring mode with a ten times magnifying lens. The roughness profile is shown in Figure 3 with the mean plane set to 0μm. The center-line average is $R_a = 0.107\mu$m, the standard deviation $\sigma = 0.143\mu$m, the skewness $Sk = -1.26$, the kurtosis $Ku = 4.50$,

the maximum of $R_p = 0.287\mu$m and the minimum of $R_v = -0.656\mu$m, where these values were calculated according to Bhushan [20].

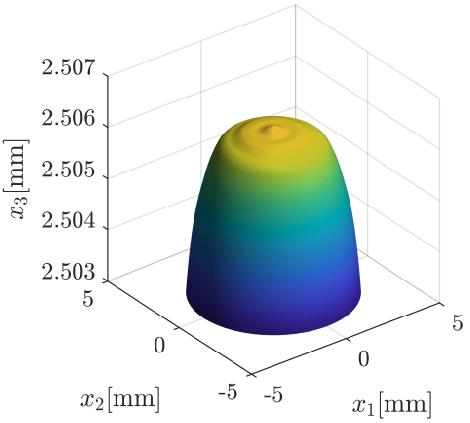

Figure 2: Macroscopic pin profile with curvature due to the polishing procedure. Note that the x_3-axis is more than 1000 times magnified in order to outline the curvature of the pin.

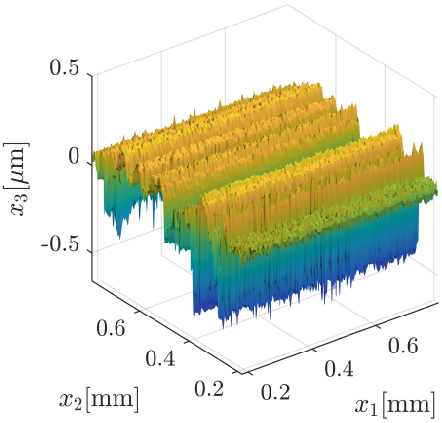

Figure 3: Representative roughness patch with grooves due to manufacturing and wear.

3. Numerical approach

3.1. Fluid mechanics

Based on the model of Wolozynski *et al.* [16] in the implementation of Codrignani *et al.* [5], the hydrodynamic pressure distribution p_{hd} in the gap of height h between pin and disc is described by the Reynolds equation considering a mass-conserving cavitation algorithm and the cavitation condition:

$$\nabla \cdot \left(h^3 \nabla p_{hd} - 6h\mu_l \begin{pmatrix} U \\ 0 \end{pmatrix} (1-\theta) \right) = 0, \tag{4}$$

$$(p_{hd} - p_{cav})\,\theta = 0. \tag{5}$$

The cavitation pressure is estimated to $p_{cav} = 0.08$MPa following [21]. The cavity fraction $\theta = 1 - \frac{\rho}{\rho_l}$ describes the amount of cavitated lubricant, where ρ_l is the density of the liquid lubricant and ρ is the density of the

mixture phase. This equation system is discretized with the finite-volume-method and solved using the Dirichlet boundary condition of ambient pressure $p_a = 101325$Pa and no cavitation at the domain boundaries. The corresponding hydrodynamic shear stress τ_{hd} on the pin surface is determined as [7]:

$$\tau_{hd} = -\frac{h}{2}\frac{\partial p_{hd}}{\partial x_1} + \frac{\mu_l U}{h}(1-\theta). \tag{6}$$

A two-scale approach is employed in order to consider the impact of roughness on the macroscopic pressure distribution while keeping the computational effort reasonable. This is achieved by evaluating the roughness effects on the microscopic scale during a preprocessing step and introducing the result as an averaged quantity in the subsequent macroscopic simulation. The macroscopic and microscopic effects are distinguished by decomposing the gap height h between pin and disc into a macroscopic gap coordinate h_0 and its microscopic variation h_r due to the roughness profile. The reference level of h_r corresponds to the mean plane of the *undeformed* roughness of the pin [22]:

$$h = h_0 + h_r. \tag{7}$$

In contrast to the pin, the disc is assumed to be perfectly flat. On the macroscopic scale of the pin, the gap coordinate h_0 is a combination of the rigid body displacement of pin and disc $h_{0,ri}$, the gap height variation due to the rigid pin geometry $h_{0,g}$ (e.g. surface curvature) and its macroscopic elastic deformation $h_{0,el}$[23]:

$$h_0 = h_{0,ri} + h_{0,g} + h_{0,el}. \tag{8}$$

The rigid body displacement of pin and disc $h_{0,ri}$ is adjusted through an iterative scheme until the load balance equation (2) is satisfied. For a value of $h_0 \leq R_p = 0.287\mu$m, surface contact between the disc and the roughness profile occurs. Since surface contact changes the roughness profile, h_0 is not an adequate description of the mean gap height during surface contact. Therefore, the meltdown gap height h_m is introduced as the distance of the disc to the mean plane of the *deformed* roughness profile on top of the pin. It is equal to h_0 for $h_0 > R_p$ but differs during surface contact. In order to determine the deformed roughness profile and meltdown gap height on the microscopic scale, it is assumed that the surface contact of disc and roughness

profile simply cuts off roughness asperities. In addition a remaining gap height of $\epsilon = 10^{-8}$m is enforced during surface contact to improve numerical stability [24]. In consequence h_m tends towards ϵ for strong surface variations. This is schematically displayed in Figure 4 and the resulting meltdown gap height as a function of the gap coordinate h_0 is shown in Figure 5. Note that h_0 can assume negative values, indicating that severe roughness deformation beyond the undeformed roughness mean plane has occured.

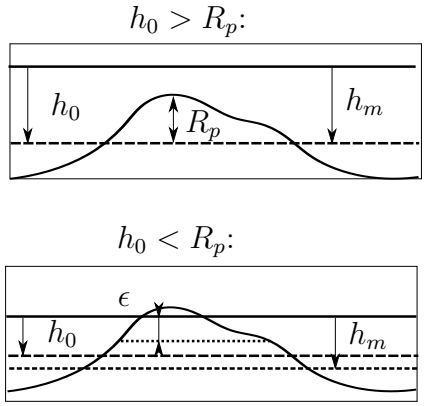

Figure 4: Schematic comparison of gap coordinate h_0 and meltdown gap height h_m with and without surface contact.

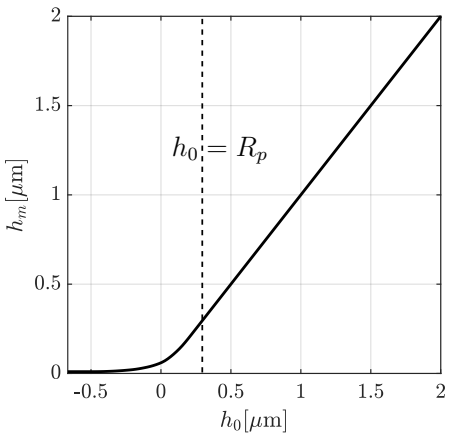

Figure 5: Meltdown gap height h_m as a function of the gap coordinate h_0 during surface contact for the specific roughness shown in Figure 3.

In the present approach, the dependency between h_m and h_0 is determined in a preprocessing step. This relationship depends only on details of the roughness geometry that is shown in Figure 3 and is determined for a number of imposed h_0 in the range between R_v and R_p. Afterwards, the Reynolds equation (4) is solved as follows. The gap coordinate h_0 is determined at each position $\vec{x}$ according to equation (8), thus representing the macroscopic geometry. Then, the roughness effects are considered through a replacement of h_0 by the previously calculated h_m as shown in Figure 5. The gap height that enters the Reynolds equation (4) is thus described by:

$$h = h_m(h_0(\vec{x})). \tag{9}$$

While using equation (9) as a description of the gap height in the Reynolds equation (4) only allows to take the average gap height over a roughness

profile into account, the homogenization of the Reynolds equation enables the consideration of the roughness's general shape and orientation [15]. Similar to the decomposition introduced by [24], this approach splits the gap height h into the meltdown gap height h_m and the corresponding *deformed* roughness gap height $h_{r,def}$, which depend on macroscopic coordinates $\vec{x}$ and roughness coordinates $\vec{\xi}$:

$$h = h(\vec{x}, \vec{\xi}) = h_m(h_0(\vec{x})) + h_{r,def}(h_0(\vec{x}), \vec{\xi}). \tag{10}$$

It is assumed that $h_{r,def}$ is periodic over the representative roughness domain $A_{\vec{\xi}}$ with the lengths Y_1 and Y_2 and that these lengths are significantly smaller than any characteristic length in the macroscopic coordinates $\vec{x}$. In this case, certain terms can be neglected when equation (10) is substituted into the Reynolds equation (4), which is after an asymptotic expansion of the hydrodynamic pressure p_{hd} averaged over the periodic domain $A_{\vec{\xi}}$. The result is the homogenized Reynolds equation and the analogously derived expression for the homogenized shear stress in dependence of the homogenization factors A, $\vec{b}$, $\vec{c}$ and d [15, 24]:

$$\nabla \cdot \left(A \nabla p_{hd} + \vec{b}\,(1-\theta) \right) = 0, \tag{11}$$

$$\tau_{hd} = \vec{c} \cdot \nabla p_{hd} + d\,(1-\theta)\,. \tag{12}$$

Summarizing, the homogenization approach for the representation of the microscale roughness is as follows: during the preprocessing, the local problems summarized in Appendix A are solved for various imposed gap coordinates h_0 and the employed roughness profile under consideration of a minimum remaining gap height of $\epsilon = 10^{-8}$m between the deformed roughness profile and the disc. From their solutions, the homogenization factors are computed as a function of the gap coordinate. This dependency of the normalized homogenization factors is displayed in Figure 6. Since the homogenization factors are normalized with the meltdown gap height h_m, the homogenization method coincides with the concept of a hydrodynamically smooth surface along the deformed roughness mean plane as long as the normalization of A_{11}, A_{22}, b_1 is equal to 1 and A_{12}, A_{21}, b_2 are equal to 0. Otherwise, the flow factors of both methods differ from each other, which becomes visible for values below $h_0 = 1\mu$m.

While the microscale is represented through the homogenization approach described above, the macroscopic pin geometry is taken into account through

the assignment of a gap coordinate h_0 to each coordinate $\vec{x}$ through equation (8). This allows solving the homogenized Reynolds equation on the macroscopic scale during the main processing.

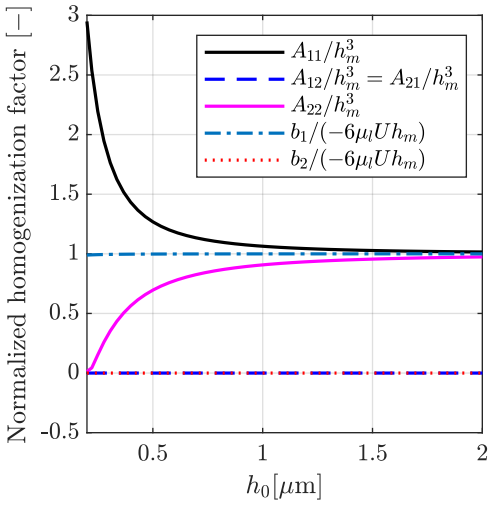

Figure 6: Normalized homogenization factors as function of the gap coordinate h_0 for the specific roughness shown in Figure 3.

3.2. Contact mechanics

In analogy to the homogenization factors, the contact pressures and shear stresses are determined during the preprocessing as a function of the gap coordinate h_0 and the employed roughness profile. For each imposed h_0, the real area of contact $A_c(h_0)$ between the roughness profile and the smooth disc is determined. Note that at this point, the earlier considered minimum remaining gap height of $\epsilon = 10^{-8}$m is not necessary for any numerical stability and therefore not employed. Tabor [25] states that the contact of two rough bodies does not actually occur on their whole macroscopic surface, but only on a small fraction of it called the real area of contact. This area is described by the contact of the surface asperities which are almost immediately plastically deformed until the real area of contact is large enough to support the whole contact load. Since almost the entire real area of contact is plastically deformed, the occurring contact pressures can be linked to the material's yield strength σ_Y. If it is further assumed that the asperities are of a small height and there is no relative movement between the surfaces, the contact

pressure p_c in a macroscopic discretization cell of area A_{tot} is described as [25]:

$$p_c = 3\sigma_Y \cdot \frac{A_c(h_0)}{A_{tot}}. \tag{13}$$

Nonetheless, first subsurface plastic deformation already occurs at a surface pressure of $1.1\sigma_Y$ [25]. However, an exact prediction about the extension of this plastically deformed subsurface volume cannot easily be made and subsurface plastic deformation is therefore omitted for the sake of a simple contact model. The precalculated contact pressure in dependence of the gap coordinate is visualized in Figure 7. Bowden and Tabor [26] also give an expression for the shear stress τ_c in the contact surface of two metals without a normal load. They explain that the metals form welded bridges which have to be sheared off by relative motion. By applying the Mises criterion of equivalent stress, the shear stress can be calculated as a function of the material's yield strength [26]:

$$\tau_c = \frac{\sigma_Y}{\sqrt{3}} \cdot \frac{A_c(h_0)}{A_{tot}} \tag{14}$$

Assuming ideal elastic-plastic material properties, the yield strength can be approximated from the Vickers hardness as described in Appendix B. It is important to mention that equation (13) assumes no shear load while equation (14) assumes no normal load. If both are present, contact and shear stresses are actually lower than those given by the equations [26]. However, these equations are used in the employed model since they excel in computation efficiency and the resulting friction coefficient in the boundary lubrication regime reflects experimental data reasonably well.

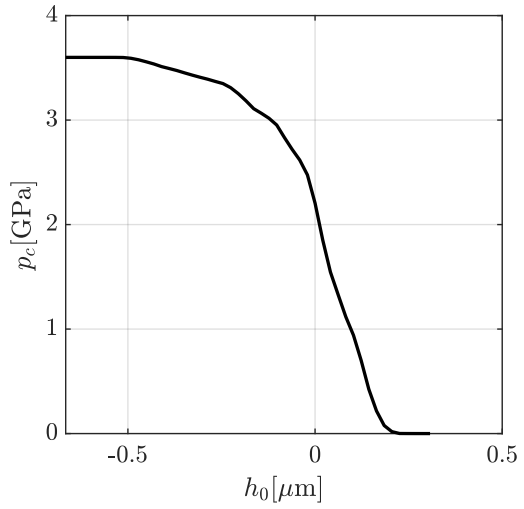

Figure 7: Contact pressure as a function of the gap coordinate. The value of $h_0 = 0$ corresponds to the roughness meltdown plane for the specific roughness shown in Figure 3.

3.3. Elastohydrodynamic deformation

The sum $p_{tot} = p_{hd} + p_c$ of the hydrodynamic and contact pressure fields elastically deforms the pin on the macroscopic scale, thereby changing the initial gap height distribution. To take this into account, the elastic deformation $h_{0,el}$ of the pin surface A is described by the elastic half-space model [17]:

$$h_{0,el}(x_1, x_2) = \frac{(1-\nu^2)}{\pi E} \iint_A \frac{p_{tot}(x_1', x_2')}{\sqrt{(x_1 - x_1')^2 + (x_2 - x_2')^2}} \mathrm{d}x_1' \mathrm{d}x_2', \tag{15}$$

where ν is Poisson's ratio and E is Young's modulus. When the surface A is discretized with the boundary element method (BEM) into rectangles, equation (15) can be expressed in dependency of a Kernel function K [17, 27]:

$$h_{0,el}(x_1, x_2) = \sum_{x_1'} \sum_{x_2'} K(x_1 - x_1', x_2 - x_2') \cdot p_{tot}(x_1', x_2'). \tag{16}$$

The computation of the elastic deformation due to a pressure field is accelerated by using the Fourier transformation $\mathcal{F}$ [17]:

$$h_{0,el} = \mathcal{F}^{-1}\left(\mathcal{F}\left(K\right) \cdot \mathcal{F}\left(p_{tot}\right)\right). \tag{17}$$

On the downside, at this point the discretized domain has to be increased and padded with zeros to perform a linear convolution instead of a circular one, which increases the computational costs of the convolution. After its calculation, the domain is resized to its old range. The resulting gap coordinate h_0 is then computed as the superposition of the rigid body displacement of pin and disc $h_{0,ri}$, the gap height variation due to the rigid pin geometry $h_{0,g}$ and its macroscopic elastic deformation $h_{0,el}$:

$$h_0(p_{tot}) = h_{0,ri} + h_{0,g} + h_{0,el}(p_{tot}). \tag{18}$$

Since h_0 depends on the total pressure profile p_{tot}, which also depends on the gap coordinate h_0, finding the equilibrium requires an iterative procedure. At first, for an initial pressure profile $p_{tot}^{(i)}$, the elastic displacement and its resulting pressure distribution $p_{tot,II}$ are computed. Then, the residuum r_{el} of the two pressure fields is calculated and the pressure field for the next iteration step $p_{tot}^{(i+1)}$ is determined by underrelaxation as long as r_{el} is higher than a threshold of $tol = 10^{-5}$:

$$r_{el} = \frac{1}{N_p} \int_{N_p} \frac{|p_{tot,II} - p_{tot}^{(i)}|}{p_a} \mathrm{d}n, \tag{19}$$

$$p_{tot}^{(i+1)} = p_{tot}^{(i)} + \alpha(p_{tot,II} - p_{tot}^{(i)}). \tag{20}$$

where N_p is the total number of the discretization points n above the pin, p_a is the ambient pressure and α is the underrelaxation factor. It is set to $\alpha = 0.5$ in the hydrodynamic and $\alpha = 0.05$ in the mixed and boundary lubrication regime to achieve a good trade-off between convergence speed and stability.

Lastly, it is important to mention that the pin geometry does not fully correspond to the half-space theory since it is loaded with pressure on all of its surface and does not have infinite extensions in any direction. This is shown in Figure 8, where the elastic pin deformation based on the BEM and caused by the pressure distribution obtained at $U = 0.8$m/s is displayed along the pin center line. This velocity was used because it marks the transition of the purely EHL to the mixed lubrication regime as explained later in section 4.1 and therefore represents a critical operating condition. A comparison is carried out between a finite element method (FEM) calculation and the previously shown BEM model by applying the same pressure distribution p_{tot} to both models (Figure 8). The FEM computation was carried out with the

software ANSYS Mechanical 2019 R3. The pin geometry was approximated as a cylinder of 2.5mm height and a radius of 4mm. Figure 9 shows the pin deformation in x_3-direction which is induced by p_{tot} at $U = 0.8$ m/s. At the sides of the pin, ambient pressure was defined, while its bottom side was assigned as a fixed support boundary condition. The deformation difference between the FEM and the BEM model can be decomposed in an offset and small shape difference. This suggests that a correction of the elastic half-space formula $h_{el,c}$ can be introduced in the following form:

$$h_{0,el,c} = a + b \cdot h_{0,el}. \tag{21}$$

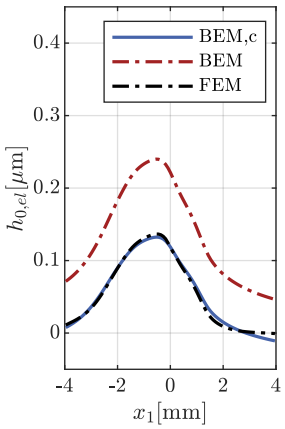

Figure 8: Elastic deformations along the pin center line as a function of the x_1-coordinate.

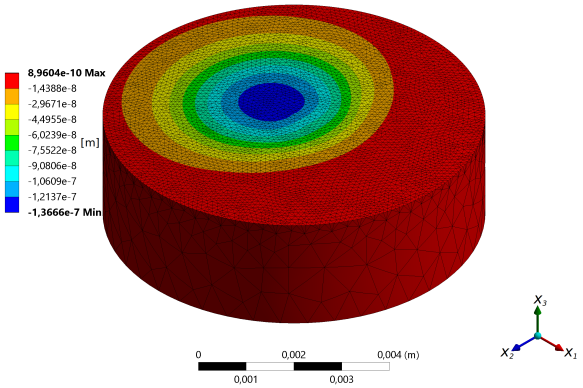

Figure 9: Elastic deformation in x_3-direction computed with FEM.

The correction constants a and b are determined by a least squares strategy so that $h_{el,c}$ fits the FEM results along the pin center line as close as possible. They come out as $a = -45.157$nm and $b = 0.7398$. The resulting corrected elastic deformation $h_{el,c}$ is also shown in Figure 8. As displayed in Figure 10, the Stribeck curves based on the uncorrected and corrected half-space formulas only differ slightly. The reason is that the difference in both elastic displacements is mainly due to the offset implied by the correction constant a. At the same time, in both cases the rigid body displacement

$h_{0,ri}$ in equation (18) is adjusted until the load balance equation (2) is satisfied. Since $h_{0,ri}$ is also a simple offset, it cancels a out. The result is that in the end, both cases have different rigid body displacements $h_{0,ri}$ and elastic deformations but nearly the same distribution of h_0. The only difference in the gap height coordinate h_0 is due to correction factor b, which is close to 1. This shows that even though the pin geometry does not correspond to a half-space, the elastic deformations can still be computed based on that assumption without introducing large errors.

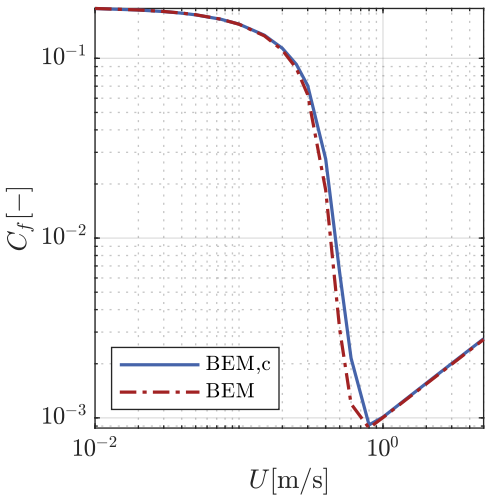

Figure 10: Stribeck curves based on the original BEM model and its corrected version.

4. Results

A digital twin of a pin-on-disc tribometer should eventually allow the prediction of Stribeck curves. While exact agreement with experimental data is challenging [5], the present model can be used to indicate potential sensitivities of the Stribeck curve to the macroscopic pin geometry and the microscopic surface roughness. Therefore, different roughness representations on the measured macroscopic pin geometry as well as variations of the macroscopic geometry are considered in the following.

The parameters used for the simulations are summarized in Table 1. In order to have a stationary numerical problem, the disc is assumed to be perfectly flat. Furthermore, the disc is considered as rigid in order to isolate EHL effects of the pin geometry.

Parameter	Value	Unit	Description
E	$206 \cdot 10^9$	Pa	Young's modulus
F_N	150	N	tribometer load force
N_p	101^2	–	number of pin discretization cells
N_r	371^2	–	number of roughness discretization cells
p_a	101325	Pa	ambient pressure
p_{cav}	80000	Pa	cavitation pressure
U	0.01...5	m/s	disc velocity
tol	10^{-5}	–	relative error tolerance
μ_l	0.0030758	$\mathrm{Pa} \cdot \mathrm{s}$	dynamic viscosity of uncavitated lubricant
ν	0.321	–	Poisson's ratio
σ_Y	$1200 \cdot 10^6$	Pa	yield strength

Table 1: Numerical parameters.

4.1. Influence of the roughness on the Stribeck curve

In section 3.1, two approaches of considering the surface roughness in the Reynolds equation were presented and will be compared in the following to investigate the roughness influence on the Stribeck curve. The first approach is simply using the meltdown gap height in the Reynolds equation. The second method consists of using the homogenized Reynolds equation. While the homogenization method allows the consideration of averaged roughness effects, it also increases the computational costs compared to just using the meltdown height gap in the Reynolds equation. The reason is a less sparse system matrix because of the off-diagonal homogenization factors in Matrix A and the additional interpolation of the homogenization factors. Based on the measured pin and roughness profiles shown in the Figures 2 and 3, the Stribeck curves are computed with both roughness methods and the obtained results are displayed Figure 11. Note that both methods use the roughness profile for the computation of the contact mechanics as described in section 3.2. Their difference is only in the consideration of roughness effects on the hydrodynamics and it can be seen that almost identical results are obtained. However, the computation using the homogenized Reynolds equation took about 3 times longer than the other one. Since roughness effects on the hydrodynamics are apparently negligible for the presently considered roughness profile, only the more efficient concept of the meltdown gap height is used in the following.

Nonetheless, it should be noted that the roughness profile is important for determining the onset of the contact pressure contribution which in turn strongly influences the transition from the purely EHL to the mixed lubrication regime. If the gap coordinate h_0 at any point $\vec{x}$ above the pin becomes less than the value of the highest roughness asperity R_p, surface contact occurs through the contribution of the contact mechanics. Thus, the transition point of the purely EHL to the mixed lubrication regime can be defined as the critical disc velocity U_c at which the minimum gap coordinate above the pin $min\left(h_0\left(\vec{x}\right)\right)$ is equal to R_p. This is visualized in Figure 12 with the results of the meltdown gap height method.

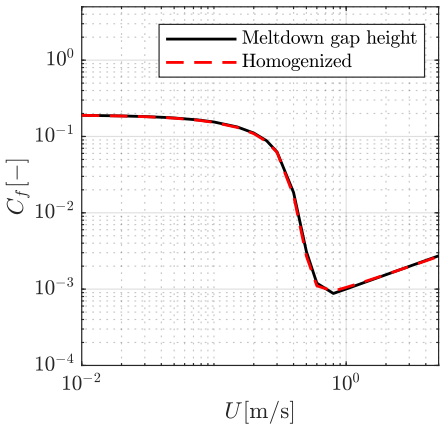

Figure 11: Stribeck curves using meltdown gap height and homogenization.

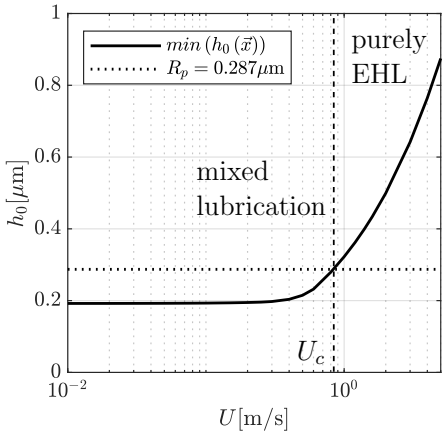

Figure 12: Minimum gap coordinate above the tribometer pin compared to R_p as a function of the disc velocity.

4.2. Influence of the pin shape on the Stribeck curve

To investigate the influence of macroscopic gap height variations, the pin profile is approximated by two parabolas. One parabola is designed to closely fit the measured pin profile in the center while the other one is chosen (within a parameter study) such that it captures the experimentally determined transition point from EHL to mixed lubrication in the Stribeck curve. The corresponding pin profiles and computed Stribeck curves are depicted in Figures 13 and 14.

The predicted friction coefficient is in very good agreement with the experimental data [8] in the boundary regime while there is a difference by

about one order magnitude in the EHL regime. This difference might be related to the neglected temperature and pressure dependence of the fluid viscosity and density on the numerical side or the low signal-to-noise-ratio of the experiment in this regime. Nonetheless, the offset indicates that the hydrodynamic model is not complete yet and must be improved in future work. Still, the model is able to indicate important sensitivities of the Reynolds equation to changes in the pin geometry. While the numerical predictions for different macroscopic pin geometries almost coincide in the EHL regime, the transition points from the purely EHL to the mixed lubrication regime and the corresponding friction coefficients show a clear dependence on the pin geometries. This dependence is further investigated in the following.

The parabola center height l_c is defined as the difference of the parabola profile height in the center of the pin to the profile height at the pin's rim. The pin parabola with a center height of $l_c = 2\mu$m is taken as a reference profile because it fits the experimental data closely. Further simulations are carried out with pin parabolas of the center heights $l_c = 1.9\mu$m, $l_c = 1.5\mu$m and $l_c = 1\mu$m. They correspond to a relative decrease of 5%, 25% and 50% of the reference center height. The resulting Stribeck curves are displayed in Figure 15. Afterwards, the change in the friction coefficient relative to the reference profile is computed for each velocity as displayed in Figure 16. It shows that a measurement deviation of 25% or 0.5μm in the characteristic length of the reference pin causes a maximum difference in the friction coefficient of more than 80%. Therefore, the observed difference between the experimentally determined Stribeck curve and the model prediction for the measured pin geometry in the mixed lubrication regime could be caused by the fact that the macroscopic pin geometry differs for a run-in pin.

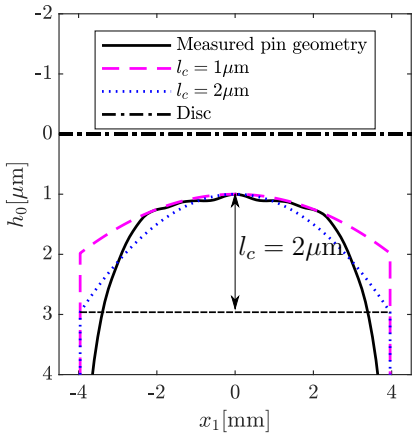

Figure 13: Gap coordinates for different pin profiles.

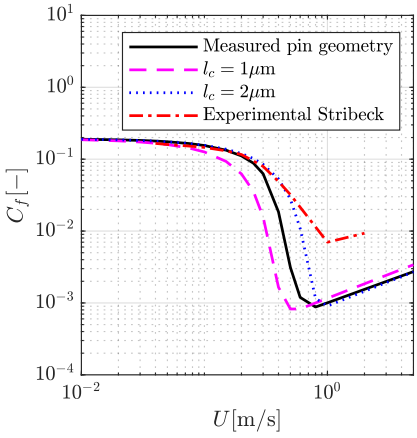

Figure 14: Stribeck curves for different pin profiles and the experimentally determined Stribeck curve of Braun *et al.* [8].

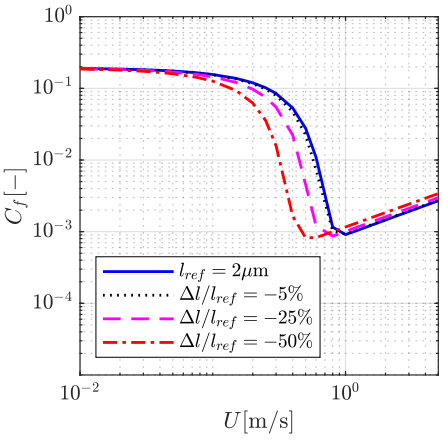

Figure 15: Stribeck curves obtained by the variation of the reference pin parabola.

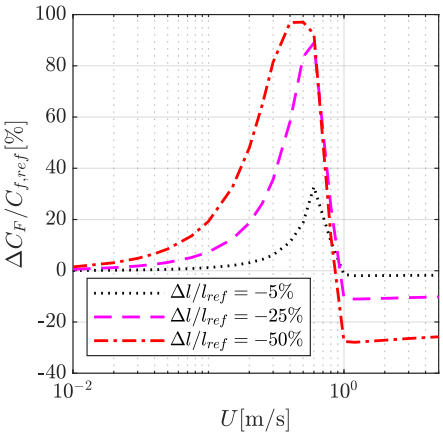

Figure 16: Relative difference in the friction coefficient compared to the reference pin parabola.

5. Conclusions

In order to investigate the sensitivity of a predicted Stribeck curve we studied the macroscopic pin shape and its microscopic roughness in a simpli-

fied digital twin of a pin-on-disc tribometer. The numerical model consists of the homogenized Reynolds equation with mass-conserving cavitation, the boundary element method and the contact mechanics model of Bowden and Tabor [25, 26]. The model is capable of simulating the tribometer in EHL, mixed and boundary lubrication conditions.

The experimental results of Braun *et al.* [8], complemented by information about the macroscopic pin geometry and surface roughness, serve as reference data for the numerically predicted Stribeck curve.

The main findings of the work can be summarized as follows:

- The measured surface roughness that is employed in this work has negligible influence on the tribometer's Stribeck curve in the EHL regime but significantly affects the relative velocity at which the transition from the purely EHL to the mixed lubrication regime occurs.

- The mixed lubrication regime of the Stribeck curve is highly sensitive to the macroscopic pin geometry. An approximation of the pin profile through a parabola allows a quantitative estimation of the pin geometry influence on the Stribeck curve. It indicates that a 0.5μm variation in the characteristic length of the pin profile can cause a deviation in the predicted friction coefficient of more than 80%.

- In order to enable the comparison of experimental results with numerical predictions, which is critical for the further development of a digital twin of a pin-on-disc-tribometer, macro- and microscopic surface measurements of the pin and disc profiles in worn conditions need to be provided.

We note that further steps to create a digital twin do not only require the knowledge of the geometric properties discussed in this work in addition to the values listed in Table 1. Moreover, the self aligning pin holder may allow variations of the pin inclination which induces changes in the gap height distribution. Also geometrical imperfections and EHL effects on the disc should be considered. Lastly, the hydrodynamic model needs to be enhanced to consider the temperature and pressure dependency of the fluid viscosity and density.

Acknowledgments

The authors want to express their gratitude to Dr.-Ing. Paul Schreiber for providing the measurements of the representative roughness used by Braun *et al.* [8]. This document is the result of a research project funded by the Friedrich und Elisabeth Boysen-Foundation.

Appendix A. Homogenization

The homogenization factors A, $\vec{b}$, $\vec{c}$ and d are determined as [15, 24]:

$$A(h_0) = \begin{pmatrix} \frac{1}{Y_1 Y_2} \int\limits_{A_{\vec{\xi}}} h^3 \left(1 + \frac{\partial \chi_1}{\partial \xi_1}\right) \mathrm{d}A_{\vec{\xi}} & \frac{1}{Y_1 Y_2} \int\limits_{A_{\vec{\xi}}} h^3 \frac{\partial \chi_2}{\partial \xi_1} \mathrm{d}A_{\vec{\xi}} \\ \frac{1}{Y_1 Y_2} \int\limits_{A_{\vec{\xi}}} h^3 \frac{\partial \chi_1}{\partial \xi_2} \mathrm{d}A_{\vec{\xi}} & \frac{1}{Y_1 Y_2} \int\limits_{A_{\vec{\xi}}} h^3 \left(1 + \frac{\partial \chi_2}{\partial \xi_2}\right) \mathrm{d}A_{\vec{\xi}} \end{pmatrix}, \tag{A.1}$$

$$\vec{b}(h_0) = \begin{pmatrix} \frac{1}{Y_1 Y_2} \int\limits_{A_{\vec{\xi}}} h^3 \frac{\partial \chi_3}{\partial \xi_1} - 6h\mu_l U \mathrm{d}A_{\vec{\xi}} \\ \frac{1}{Y_1 Y_2} \int\limits_{A_{\vec{\xi}}} h^3 \frac{\partial \chi_3}{\partial \xi_2} \mathrm{d}A_{\vec{\xi}} \end{pmatrix}, \tag{A.2}$$

$$\vec{c}(h_0) = \begin{pmatrix} \frac{1}{Y_1 Y_2} \int\limits_{A_{\vec{\xi}}} -\frac{h}{2} \left(1 + \frac{\partial \chi_1}{\partial \xi_1}\right) \mathrm{d}A_{\vec{\xi}} \\ \frac{1}{Y_1 Y_2} \int\limits_{A_{\vec{\xi}}} -\frac{h}{2} \frac{\partial \chi_2}{\partial \xi_1} \mathrm{d}A_{\vec{\xi}} \end{pmatrix}, \tag{A.3}$$

$$d(h_0) = \frac{1}{Y_1 Y_2} \int\limits_{A_{\vec{\xi}}} -\frac{h}{2} \frac{\partial \chi_3}{\partial \xi_1} + \frac{\mu_l U}{h} \mathrm{d}A_{\vec{\xi}}. \tag{A.4}$$

Bayada *et al.* [15] only employed longitudinal, transversal or oblique roughness profiles and could therefore derive an analytical solution of the homogenization factors. In order to consider arbitrary roughness profiles, the following local problems must be solved numerically for their solutions χ_1, χ_2 and χ_3 in [24]:

$$\nabla_{\vec{\xi}} \cdot \left(h^3 \nabla_{\vec{\xi}} \chi_1\right) = -\frac{\partial h^3}{\partial \xi_1}, \tag{A.5}$$

$$\nabla_{\vec{\xi}} \cdot \left(h^3 \nabla_{\vec{\xi}} \chi_2\right) = -\frac{\partial h^3}{\partial \xi_2}, \tag{A.6}$$

$$\nabla_{\vec{\xi}} \cdot \left(h^3 \nabla_{\vec{\xi}} \chi_3\right) = 6\mu_l U \cdot \frac{\partial h}{\partial \xi_1}. \tag{A.7}$$

The indexed nabla operator $\nabla_{\vec{\xi}}$ means using it with respect to the $\vec{\xi}$ coordinates.

Appendix B. Relation of Vickers hardness and yield strength

Depending on whether the Vickers hardness is calculated from the indentation mass or force, there are two slightly different hardness definitions.

Tabor describes the Vickers hardness HV_T as [25]:

$$HV_T = \frac{W}{A_S} = 0.9272\frac{W}{A_G} = 1.8544\frac{W}{d^2}, \tag{B.1}$$

where W is the applied indentation mass in kg and A_S is the area of the sides of the indented volume. For a Vickers indentation pyramid, $A_S = A_G/0.927$ holds, where $A_G = d^2/2$ is the projected surface of the indented volume. The diagonal length of A_G is given by d in mm. The resulting hardness HV_T has the units kg/mm^2. In this case, the ultimate tensile strength in MPa roughly correlates to:

$$UTS \approx 3HV_T \cdot \mathrm{m/s^2}. \tag{B.2}$$

However, there exists another definition of the Vickers hardness HV in dependency of the indentation force F_I in the unit N, which is commonly used e.g. in Germany [28]:

$$HV = 0.189\frac{F_I}{d^2}. \tag{B.3}$$

From experiments, an approximation for the ultimate tensile strength in MPa was found [28]:

$$UTS \approx 3HV. \tag{B.4}$$

In both cases, the yield strength is equal to the ultimate tensile strength $\sigma_y = UTS$ if ideal elastic-plastic material properties are assumed.

References

[1] K. Holmberg, A. Erdemir, The impact of tribology on energy use and CO2 emission globally and in combustion engine and electric cars, Tribology International 135 (2019) 389–396.

[2] D. Gropper, L. Wang, T. J. Harvey, Hydrodynamic lubrication of textured surfaces: A review of modeling techniques and key findings, Tribology International 94 (2016) 509–529.

[3] I. Etsion, State of the art in laser surface texturing, Journal of Tribology 127 (1) (2005) 248–253.

[4] M. B. Dobrica, M. Fillon, About the validity of Reynolds equation and inertia effects in textured sliders of infinite width, Proceedings of the Institution of Mechanical Engineers, Part J: Journal of Engineering Tribology 223 (1) (2009) 69–78.

[5] A. Codrignani, B. Frohnapfel, F. Magagnato, P. Schreiber, J. Schneider, P. Gumbsch, Numerical and experimental investigation of texture shape and position in the macroscopic contact, Tribology International 122 (2018) 46–57.

[6] A. Dadouche, M. Fillon, W. Dmochowski, Performance of a hydrodynamic fixed geometry thrust bearing: comparison between experimental data and numerical results, Tribology Transactions 49 (3) (2006) 419–426.

[7] F. Profito, S.-C. Vladescu, T. Reddyhoff, D. Dini, Experimental validation of a mixed-lubrication regime model for textured piston-ring-liner contacts, Materials Performance and Characterization 6 (2) (2017) 112–129.

[8] D. Braun, C. Greiner, J. Schneider, P. Gumbsch, Efficiency of laser surface texturing in the reduction of friction under mixed lubrication, Tribology International 77 (2014) 142–147.

[9] J. Schneider, D. Braun, C. Greiner, Laser textured surfaces for mixed lubrication: influence of aspect ratio, textured area and dimple arrangement, Lubricants 5 (3) (2017) 32.

[10] D. Z. Segu, P. Hwang, Friction control by multi-shape textured surface under pin-on-disc test, Tribology International 91 (2015) 111–117.

[11] B. Podgornik, L. Vilhena, M. Sedlaček, Z. Rek, I. Žun, Effectiveness and design of surface texturing for different lubrication regimes, Meccanica 47 (7) (2012) 1613–1622.

[12] H. Zhang, D. Zhang, M. Hua, G. Dong, K. Chin, A study on the tribological behavior of surface texturing on babbitt alloy under mixed or starved lubrication, Tribology Letters 56 (2) (2014) 305–315.

[13] A. Kovalchenko, O. Ajayi, A. Erdemir, G. Fenske, I. Etsion, The effect of laser surface texturing on transitions in lubrication regimes during unidirectional sliding contact, Tribology International 38 (3) (2005) 219–225.

[14] R. Larsson, Modelling the effect of surface roughness on lubrication in all regimes, Tribology International 42 (4) (2009) 512–516.

[15] G. Bayada, S. Martin, C. Vázquez, An average flow model of the Reynolds roughness including a mass-flow preserving cavitation model, Journal of Tribology 127 (4) (2005) 793.

[16] T. Woloszynski, P. Podsiadlo, G. W. Stachowiak, Efficient solution to the cavitation problem in hydrodynamic lubrication, Tribology Letters 58 (1) (2015) 839.

[17] R. Pohrt, Q. Li, Complete boundary element formulation for normal and tangential contact problems, Physical Mesomechanics 17 (4) (2014) 334–340.

[18] A. R. Codrignani, Numerical representation of a pin-on-disc tribometer for the investigation of textured surfaces, Ph.D. thesis, Karlsruhe Institute of Technology (2018).

[19] C. Greiner, T. Merz, D. Braun, A. Codrignani, F. Magagnato, Optimum dimple diameter for friction reduction with laser surface texturing: the effect of velocity gradient, Surface Topography: Metrology and Properties 3 (4) (2015) 044001.

[20] B. Bhushan, Surface roughness analysis and measurement techniques, in: Modern Tribology Handbook, Two Volume Set, CRC press, 2000, pp. 79–150.

[21] C. Shen, M. Khonsari, On the magnitude of cavitation pressure of steady-state lubrication, Tribology Letters 51 (1) (2013) 153–160.

[22] A. Almqvist, R. Larsson, P. Wall, The homogenization process of the time dependent reynolds equation describing compressible liquid flow, Tribologia: Finnish Journal of Tribology 26 (4) (2007) 30–44.

[23] C. H. Venner, A. A. Lubrecht, Multi-level methods in lubrication, Elsevier, 2000.

[24] F. Sahlin, R. Larsson, A. Almqvist, P. Lugt, P. Marklund, A mixed lubrication model incorporating measured surface topography. Part 1: theory of flow factors, Proceedings of the Institution of Mechanical Engineers, Part J: Journal of Engineering Tribology 224 (4) (2009) 335–351.

[25] D. Tabor, The Hardness of Metals, At the Clarendon Press, Oxford, 1951.

[26] F. P. Bowden, D. Tabor, The Friction and Lubrication of Solids, 2nd Edition, At the Clarendon Press, Oxford, 1954.

[27] A. E. H. Love, The stress produced in a semi-infinite solid by pressure on part of the boundary, Philosophical Transactions of the Royal Society of London. Series A, Containing Papers of a Mathematical or Physical Character 228 (659-669) (1929) 377–420.

[28] W. Weissbach, M. Dahms, C. Jaroschek, Werkstoffe und ihre Anwendungen : Metalle, Kunststoffe und mehr, Springer Vieweg, Wiesbaden, 2018.